

---

# MixQuant: Pushing the Limits of Block Rotations in Post-Training Quantization

---

Sai Sanjeet<sup>12\*</sup>, Ian Colbert<sup>1\*</sup>, Pablo Monteagudo-Lago<sup>1</sup>, Giuseppe Franco<sup>1</sup>, Yaman Umuroglu<sup>1</sup>, Nicholas J. Fraser<sup>1</sup>

<sup>1</sup>Advanced Micro Devices, Inc. (AMD)

<sup>2</sup>Dept. of Electrical Engineering, State University of New York at Buffalo

## ABSTRACT

Activation outliers remain a major barrier to obtaining accurate few-bit language models. Recent post-training quantization (PTQ) methods insert rotations into the compute graph to diffuse these outliers across vector coordinates prior to rounding. Importantly, while many rotations can be merged into model weights offline, others must be evaluated online, incurring non-trivial inference overhead. To reduce this cost, recent work adopts block rotations, where fixed-size partitions of a vector are rotated independently. Although smaller blocks are known to reduce overhead, the impact of block structure on outlier suppression remains poorly understood. To fill this gap, we provide the first systematic, non-asymptotic analysis of outlier suppression for block Hadamard rotations. We first derive deterministic sufficient conditions under which block Hadamard rotations suppress outliers. We then prove that reducing block size can worsen post-rotation outliers with high probability, revealing a trade-off with computational cost. Furthermore, our analysis also reveals that outlier suppression is fundamentally limited by the geometry of the input vector. In particular, post-rotation outliers are deterministically minimized when the pre-rotation  $\ell_1$  norm mass is evenly distributed across blocks. Guided by these insights, we introduce MixQuant, a block rotation-aware PTQ framework that redistributes activation mass via permutations prior to rotation. To calibrate the permutations, we propose a greedy mass diffusion algorithm that equalizes the expected  $\ell_1$  norms across blocks. To avoid adding inference overhead, we identify permutation-equivariant regions in transformer architectures to merge the resulting permutations into model weights before deployment. Our experiments show that MixQuant consistently improves accuracy across all block sizes; for example, when quantizing Llama3 1B to INT4 with block sizes of 16, MixQuant recovers up to 90% of the full-vector rotation perplexity, compared to 46% recovery without permutations.

## 1 Introduction

Post-training quantization (PTQ) remains essential for improving the efficiency of large language models (LLMs), yet activation outliers continue to limit model accuracy in few-bit settings. Recent methods insert rotations into the compute graph to diffuse these outliers across vector coordinates, often substantially improving accuracy. However, while some rotations can be merged into model weights before deployment, others must be computed online during inference, incurring non-trivial runtime overheads. For example, Ashkboos *et al.* [1] report 7-15% latency overhead from online rotations when running Llama2 7B at INT4.

A natural approach to reduce the cost of online rotations is to partition activation vectors into fixed-sized blocks and apply rotations independently within each block. When the rotations are Hadamard matrices, this reduces compute requirements from  $\mathcal{O}(d \log d)$  to  $\mathcal{O}(d \log b)$  for a  $d$ -dimensional activation vector and block size  $b$ . In practice, this can yield meaningful runtime improvements: Shao *et al.* [2] report a  $1.5 \times$  reduction in online rotation overhead when replacing full-vector Hadamard rotations with block Hadamard rotations with  $b = 32$  for Llama2 7B running at MXFP4, corresponding to a 2% reduction in end-to-end latency. However, this efficiency gain is not free. We prove that reducing block size  $b$  can increase worst-case post-rotation outliers with high probability, later formalized in Proposition 3.5.

---

\*Equal contribution. Correspondence to: [syerragu@buffalo.edu](mailto:syerragu@buffalo.edu), [ian.colbert@amd.com](mailto:ian.colbert@amd.com)

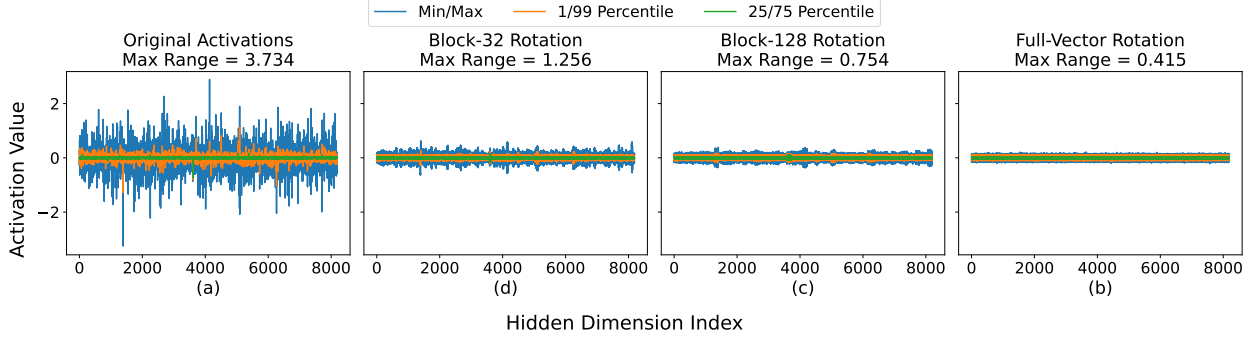


Figure 1: We visualize input activation distributions sampled from 2048 tokens of WikiText2 at the third down projection layer in Llama3 1B under four configurations: (a) original model, (b) block Hadamard rotation with  $b = 32$ , (c) block Hadamard rotation with  $b = 128$ , and (d) full-vector rotation. As  $b \rightarrow d$ , the activation range decreases, showing block rotations can reduce outlier suppression effectiveness.

Figure 1 illustrates this effect within Llama3 1B: while full-vector rotations substantially reduce activation ranges, smaller block rotations are often less effective at suppressing outliers. As a result, block rotations can introduce a trade-off between computational efficiency and model accuracy for quantized LLMs. In this work, we identify and mitigate fundamental limitations of block Hadamard rotations to improve outlier suppression while retaining efficiency.

**Contributions.** We introduce MixQuant, a new framework for calibrating permutations to improve the outlier suppression capabilities of block rotations for few-bit LLM inference. Our work is driven by three key contributions. **First**, we present the first systematic, non-asymptotic analysis of the outlier suppression capabilities of full-vector and block Hadamard rotations. Prior work asymptotically analyzes expected  $\ell_2$  error after block rotations [3], offering insights under Laplacian or Gaussian assumptions but no worst-case guarantees. In contrast, our analysis yields the first deterministic bounds that provide sufficient conditions under which full-vector and block Hadamard rotations suppress outliers (Propositions 3.1 and 3.3). Our analysis reveals that outlier suppression is fundamentally limited by the geometry of the input vector, namely its  $\ell_1$  norm mass distribution. Moreover, we analyze how these limits evolve with block size, both deterministically (Corollary 3.4) and probabilistically (Proposition 3.5). **Second**, we propose a greedy mass diffusion algorithm (MassDiff) that uses calibration data to construct permutation matrices to equalize full-precision activation mass across blocks prior to rotation and rounding. **Third**, we show that permutations can be merged into surrounding layers by identifying and exploiting permutation-equivariant regions in neural network architectures, yielding an end-to-end framework that improves the outlier suppression capabilities of block Hadamard rotations without introducing additional inference-time overhead. In Section 5, we show that MixQuant consistently improves the accuracy of few-bit models compared to existing baselines, completely closing the gap to full-vector rotations with block sizes of 128 or higher.

**Notation.** Throughout the paper, a  $d$ -dimensional input activation  $X \in \mathbb{R}^d$  is a row vector, where  $d = nb$  for  $n$  blocks of  $b$  elements. The  $j$ -th block of  $X$  is denoted  $X_{\{j\}} \in \mathbb{R}^b$  for  $j \in [n]$ , where  $[n] = \{1, \dots, n\}$ .  $R \in \mathbb{R}^{k \times k}$  denotes a normalized Hadamard matrix, where  $R_i \in \mathbb{R}^k$  denotes the  $i$ -th column of  $R$  with  $\|R_i\|_2 = 1$  and  $\|R_i\|_\infty = 1/\sqrt{k}$  for  $i \in [k]$ . A block rotation is the block-diagonal matrix constructed via the Kronecker product  $\tilde{R} = I_n \otimes R = \text{diag}(R, \dots, R)$ , where  $I_n \in \mathbb{R}^{n \times n}$  is the identity matrix. Note that  $\tilde{R} \in \mathbb{R}^{d \times d}$  when  $k = b$ . A matrix  $P \in \mathbb{R}^{d \times d}$  is a permutation matrix if there exists a permutation  $\pi : [d] \rightarrow [d]$  such that  $P e_i = e_{\pi(i)}$  for all  $i \in [d]$ ; equivalently, each row and column of  $P$  contains exactly one entry equal to 1, with all other entries equal to 0. Finally, a quantizer  $\mathcal{Q} : \mathbb{R} \rightarrow \mathcal{A}$  maps real values to a discrete  $q$ -bit alphabet  $\mathcal{A} \subset \mathbb{Z}$ , where  $|\mathcal{A}| = 2^q$ . We specify the quantizers used for the data formats studied in this work in Appendix B.

## 2 Background and Related Work

Recent advances in post-training quantization (PTQ) can be broadly organized into two stages of a quantization pipeline, as illustrated in Figure 2. The first involves applying transformations to the full-precision weights or activations. The second involves mapping the resulting weights or activations to a discrete target alphabet (e.g., 4-bit integers), typically via error-correcting rounding algorithms. Our work focuses on the first stage.

**Transformation algorithms.** Several recent works propose applying transformations to the weights and activations of a full-precision model prior to rounding. Depending on how transformations are incorporated into the compute graph, they may either be merged into model tensors as an offline preprocessing step before deployment, or remain

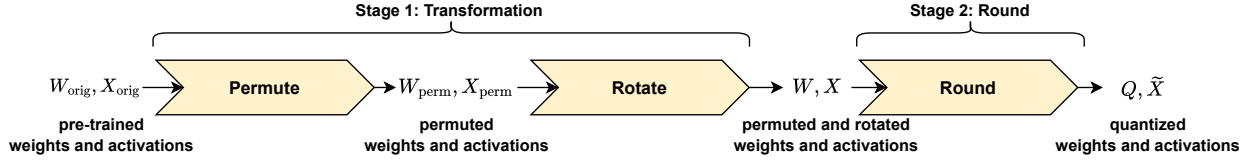


Figure 2: Given pre-trained weights and activations, MixQuant first computes a permutation that equalizes the per-block activation mass. The permuted weights and activations are then rotated. Finally, the permuted and rotated weights and activations are then rounded to a target alphabet defined by a bit width, scaling factor, and zero point.

explicitly in the graph to be evaluated at inference time. We refer to the former as *mergeable* and the latter as *online*. One line of work equalizes dynamic range within scale-equivariant regions of a compute graph. Prominent examples include SmoothQuant [4] and AWQ [5], which propose strategies to redistribute dynamic range from the activations to the weights by calibrating mergeable, channelwise scales prior to rounding. Another line of work inserts rotations into the graph prior to rounding to suppress outliers in both the weights and activations. These rotations may be random [1, 6], expandable [7, 8], or learned [9, 10]. When rotations are mergeable, they can be applied without impacting inference-time computation. In contrast, online rotations can incur significant inference overhead, especially in high-dimensional layers (see Remark 3.2). This cost motivates the study of structured rotation schemes that trade expressivity for computational efficiency while preserving the outlier suppression benefits of dense full-vector rotations.

**Structured rotations.** Early works using online rotations, such as QuIP [6], adopt random dense orthonormal matrices, requiring  $\mathcal{O}(d^2)$  operations to rotate an activation vector  $X \in \mathbb{R}^d$ . One line of work reduces this complexity by imposing algebraic structure on full-vector rotations. For example, FlatQuant [11] learns Kronecker decompositions of dense matrices, reducing the cost to  $\mathcal{O}(d\sqrt{d})$ . Other approaches further restrict structure: QuaRot [1] adopts random Hadamard rotations and ButterflyQuant [12] learns butterfly factorizations of Givens matrices, both admitting  $\mathcal{O}(d \log d)$  implementations. A complementary strategy is to independently apply rotations to fixed-size partitions of  $X$ , yielding block rotations. DuQuant [13] composes dense block rotations with permutations, reducing memory to  $\mathcal{O}(b^2)$  for block size  $b$  while requiring  $\mathcal{O}(db)$  operations at inference. In practice, block Hadamard rotations have emerged as the most common structured rotation, reducing the computational cost to  $\mathcal{O}(d \log b)$ . Recent works such as MR-GPTQ [3] and BRQ [2] study block Hadamard rotations with microscaled (MX) datatypes, underscoring their practical relevance in modern PTQ pipelines. Our work takes a complementary perspective. Rather than proposing a new family of structured rotations or focusing on their interaction with specific numerical formats, we analyze the outlier suppression capabilities of Hadamard rotations, and use the resulting insights to design an equalization framework that maintains these capabilities under block structure constraints.

### 3 A Theoretical Analysis of When (Block) Rotations Suppress Outliers

The connection between outlier suppression and quantization error can be seen through deterministic worst-case bounds. For integer quantizer  $\mathcal{Q}$ , the step size (or scaling factor) is commonly defined as  $s = \|X\|_\infty / (2^{q-1} - 1)$  for a  $q$ -bit alphabet [14]. The worst-case quantization error for activation vector  $X \in \mathbb{R}^d$  satisfies

$$\|X - \mathcal{Q}(X)\|_\infty \leq \frac{1}{2^q - 2} \|X\|_\infty \quad \text{and} \quad \|X - \mathcal{Q}(X)\|_2 \leq \frac{\sqrt{d}}{2^q - 2} \|X\|_\infty.$$

Indeed, the worst-case quantization error is known to scale linearly with  $\|X\|_\infty$  [15, 16], so suppressing outliers (*i.e.*, reducing  $\|X\|_\infty$ ) directly tightens worst-case  $\ell_\infty$  and  $\ell_2$  error.

Using this lens, we first establish sufficient conditions under which full-vector Hadamard rotations suppress outliers (Proposition 3.1). We then generalize our analysis to block Hadamard rotations (Proposition 3.3), and characterize how worst-case post-rotation outliers evolve with block size both deterministically (Corollary 3.4) and probabilistically (Proposition 3.5). All proofs are provided in Appendix D.

#### 3.1 Outlier Suppression with Full-Vector Hadamard Rotations

We first offer a deterministic and non-asymptotic characterization of when full-vector Hadamard rotations suppress outliers in activation vector  $X$ , starting with the following proposition.

**Proposition 3.1** (When Full-Vector Hadamard Rotations Suppress Outliers). *Let  $X \in \mathbb{R}^d$  be an activation vector, and let  $R \in \mathbb{R}^{d \times d}$  be a normalized Hadamard matrix. Define  $\delta = \|X\|_1 / (d\|X\|_\infty)$ , then the rotation of  $X$  by  $R$  satisfies*

$$\|XR\|_\infty \leq \delta\sqrt{d}\|X\|_\infty. \quad (1)$$

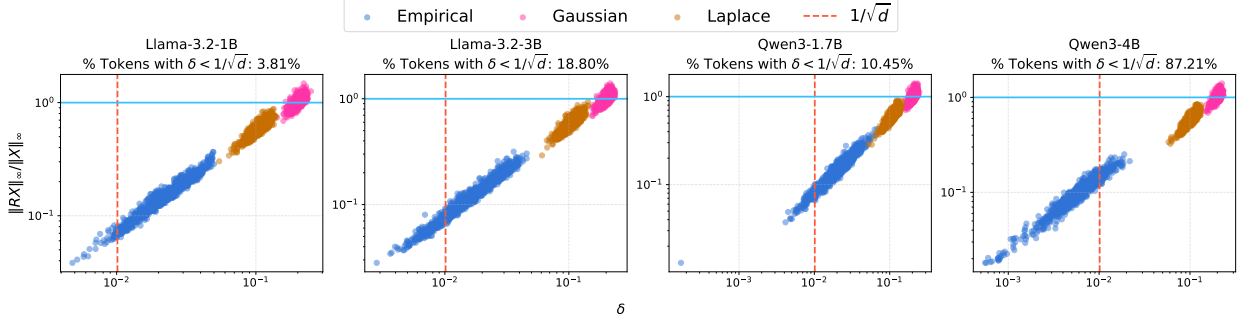


Figure 3: In **blue**, we show the values of  $\delta$  and the normalized post-rotation range  $\|XR\|_\infty/\|X\|_\infty$  for 1024 tokens sampled from the third down projection layer of Llama3 [17] and Qwen3 [18] models, using activations from WikiText2 [19]. The reference value  $1/\sqrt{d}$  is shown in **red**, below which Proposition 3.1 guarantees range reduction. Although most tokens lie above this sufficient threshold, range reduction is observed consistently, and the degree of reduction is strongly correlated with  $\delta$ . For comparison, **Gaussian** and **Laplacian** distributions are first fit to the empirical activations on a per-token basis, and  $\delta$  values are then computed from samples drawn from these fitted distributions; their resulting  $\delta$  distributions differ substantially from those observed for real LLM activations.

Intuitively, the degree of outlier suppression varies with the geometry of  $X$  as captured by  $\delta$ , which can be interpreted as the concentration of  $\ell_1$  norm mass in  $X$ . Since  $\|X\|_\infty \leq \|X\|_1 \leq d\|X\|_\infty$ , we have  $\delta \in [d^{-1}, 1]$ . Larger values of  $\delta$  correspond to vectors of near-uniform magnitude, whereas smaller values of  $\delta$  correspond to vectors dominated by a few large outliers. The latter is common in modern language models, whose activations typically exhibit increasing kurtosis as models scale in size [20]. Equation 1 therefore offers a concrete explanation for why rotation-based transformation methods empirically succeed at suppressing outliers and improving quantization accuracy.

Our bound also yields a clear guarantee:  $\|XR\|_\infty < \|X\|_\infty$  when  $\delta < 1/\sqrt{d}$ . Importantly, this condition is sufficient but not necessary; outlier suppression can and does occur in practice for activation vectors with  $\delta$  well above this threshold. Figure 3 visualizes the empirical behavior of  $\delta$  for Llama3 and Qwen3 models, showing that activation range is consistently reduced across all sampled tokens even when the sufficient condition is not satisfied. Moreover, Figure 3 provides two additional insights. First, the empirical distribution of  $\delta$  for real LLM activations differs markedly from those implied by common distributional assumptions. To ensure a fair comparison, Gaussian and Laplacian models are fit to the empirical activations on a per-token basis, and  $\delta$  values are then computed from samples drawn from these fitted distributions. The resulting distributions fail to capture the empirical distribution of mass concentration observed in real models, highlighting the limits of analyses based on such assumptions. Second,  $\delta$  is strongly correlated with the normalized post-rotation range  $\|XR\|_\infty/\|X\|_\infty$ , indicating that mass concentration serves as an effective proxy for predicting the degree of outlier suppression achieved by rotation.

### 3.2 Outlier Suppression with Block Hadamard Rotations

The preceding analysis establishes, both theoretically and empirically, that full-vector Hadamard rotations can strongly suppress outliers. However, as discussed in Section 2, existing methods often require inserting online rotations into the compute graph to exploit these benefits, introducing inference overhead. Although optimized implementations of Hadamard rotations exist [21, 22], this overhead remains non-negligible [1]. An emerging response is to restrict full-vector Hadamard rotations to operate on smaller partitions of an activation vector via block Hadamard rotations [2, 3]. The following remark summarizes the compute requirements of full-vector and block Hadamard rotations.

**Remark 3.2** (Compute Requirements of Hadamard Rotations). Consider applying a Hadamard rotation to an activation vector of dimension  $d = kt$ , where  $t$  is the largest factor of  $d$  that is not a power of two and  $k$  is the remaining power-of-2 component. When  $t = 1$ , then  $d$  is a power of 2 and the Hadamard rotation can be implemented via a butterfly decomposition with  $\mathcal{O}(d \log d)$  operations [21]. However, for  $t > 1$ , the standard butterfly decomposition does not directly apply. In Appendix A, we show that a non-power-of-2 Hadamard rotation can be reduced to complexity  $\mathcal{O}(dt + d \log k)$ . Consequently, for any  $d$ , full-vector online Hadamard rotations incur at least  $\mathcal{O}(d \log d)$  compute cost, which becomes significant at the large activation dimensions encountered in state-of-the-art LLM architectures. This motivates restricting online rotations to operate on smaller, power-of-2 partitions as a general strategy for reducing inference-time computation. Accordingly, a block Hadamard rotation with block size  $b$  applies independent Hadamard rotations within each block and has complexity  $\mathcal{O}(d \log b)$ , yielding substantial compute savings when  $b \ll d$ .

Table 1: We present the minimum compute operations (additions and subtractions) required to apply full-vector and block Hadamard rotations to the down projection layer inputs in Llama3 and Qwen3 models. For each model, we list the dimension  $d$  of the input activations, its decomposition into power-of-2 and non-power-of-two components  $k$  and  $t$ , respectively, and the operation counts for block sizes  $b \in \{32, 128, 512\}$  relative to full-vector rotations.

Model	Size	$d$	$k$	$t$	32	128	512	Full
Llama3	1B/3B	8192	$2^{13}$	1	40960 (38%)	57344 (54%)	73728 (69%)	106496
	8B	14336	$2^{11}$	7	71680 (28%)	100352 (39%)	129024 (50%)	258048
Qwen3	1.7B	6144	$2^{11}$	3	30720 (36%)	43008 (50%)	55296 (64%)	86016
	4B	9728	$2^9$	19	48640 (18%)	68096 (25%)	87552 (32%)	272384
	8B	12288	$2^{12}$	3	61440 (33%)	86016 (47%)	110592 (60%)	184320

Table 1 reports the minimum compute operations required to rotate the input activations of down projection layers in various Llama3 and Qwen3 models with full-vector or block Hadamard rotations.<sup>2</sup> Across models, restricting rotations to smaller blocks substantially reduces the compute requirements of online rotations. At the same time, restricting Hadamard rotations to operate on fixed-size partitions of an activation vector fundamentally changes how mass is redistributed across coordinates. The following proposition formalizes this effect by characterizing when block Hadamard rotations suppress outliers, and how this capability depends on block size.

**Proposition 3.3** (When Block Hadamard Rotations Suppress Outliers). *Let  $\tilde{R} = I_n \otimes R$  be a block rotation, where  $R \in \mathbb{R}^{b \times b}$  is a normalized Hadamard matrix and  $\tilde{R} \in \mathbb{R}^{d \times d}$  with  $d = nb$ . Let  $X_{\{j\}} \in \mathbb{R}^b$  be the  $j$ -th block of activation vector  $X \in \mathbb{R}^d$  for  $j \in [n]$ . Define  $\delta_{\{j\}} = \|X_{\{j\}}\|_1 / (b\|X_{\{j\}}\|_\infty)$ , then the rotation of  $X$  by  $\tilde{R}$  satisfies*

$$\|X\tilde{R}\|_\infty \leq \max_{j \in [n]} \delta_{\{j\}} \sqrt{b} \|X_{\{j\}}\|_\infty. \quad (2)$$

Proposition 3.3 provides a principled characterization of when block Hadamard rotations suppress outliers. Importantly, it strictly subsumes Proposition 3.1; Equation 2 reduces exactly to Equation 1 as  $b \rightarrow d$ . Moreover, since  $\delta_{\{j\}}\|X_{\{j\}}\|_\infty = \|X_{\{j\}}\|_1/b$ , outlier suppression in the block setting is fundamentally limited by the local geometry of the activation vector, namely the block with the largest  $\ell_1$  norm mass. This dependence is captured by the per-block ratio  $\delta_{\{j\}} \in [b^{-1}, 1]$ , which plays the same role as  $\delta$  in the full-vector case but is now tied to both the block size  $b$  and the local geometry within each block. For a fixed block size  $b$ , larger values of  $\delta_{\{j\}}$  correspond to blocks whose coordinates are more evenly distributed. Therefore, the bound in Equation 2 is dominated by blocks that exhibit both (1) high intra-block uniformity (large  $\delta_{\{j\}}$ ) and (2) large  $\|X_{\{j\}}\|_\infty$  relative to  $\|X\|_\infty$ . For a fixed activation vector  $X$ , one can reason mechanistically about how outlier suppression evolves with block size via the following corollary.

**Corollary 3.4** (Deterministic Evolution of Post-Rotation Outliers). *Let  $X \in \mathbb{R}^d$  be an activation vector and let  $X_{\{j\}} \in \mathbb{R}^b$  be the  $j$ -th block of  $X$  for  $j \in [n]$  with  $d = nb$ . Define  $\mathcal{Z}(b; X) = \max_{j \in [n]} \sqrt{b} \delta_{\{j\}} \|X_{\{j\}}\|_\infty$ , where  $\delta_{\{j\}} = \|X_{\{j\}}\|_1 / (b\|X_{\{j\}}\|_\infty)$ . Then, for positive integers  $k, b' \in \mathbb{N}$  such that  $b = kb'$ , it is verified that*

$$\mathcal{Z}(b; X) \leq \sqrt{k} \mathcal{Z}(b'; X)$$

Given activation vector  $X$  and an atomic block size  $b'$ , the worst-case post-rotation outlier increases by a factor of  $\sqrt{k}$  as the block size is increased to  $b = kb'$ . This behavior reflects the inherent pessimism of a worst-case analysis: increasing  $b$  increases the number of terms contributing to each rotated coordinate and, in the worst case, their signs can constructively align with the Hadamard matrix. While this deterministic perspective is informative, it does not explicitly capture the behavior encountered in practice as the interaction between the block structure of rotation  $\tilde{R}$  and the local geometry of activation  $X$  is non-trivial.

To better understand the expected behavior of Equation 2, we visualize the empirical relationship between  $\max_j \delta_{\{j\}} \|X_{\{j\}}\|_\infty / \|X\|_\infty$  and block size  $b$  in Figure 4. By definition,  $\delta_{\{j\}} \geq b^{-1}$ , so this quantity is lower bounded by  $1/b$ . Moreover, as in Proposition 3.1, Proposition 3.3 yields a sufficient condition for guaranteed outlier suppression:  $\|X\tilde{R}\|_\infty < \|X\|_\infty$  when  $\max_j \delta_{\{j\}} \|X_{\{j\}}\|_\infty / \|X\|_\infty < 1/\sqrt{b}$ . Across all down projection layers of the

<sup>2</sup>The full-vector costs depend strongly on the largest non-power-of-2 factor of the activation dimension, which can lead to higher operation counts even for smaller vectors (e.g., Qwen3 4B vs. Qwen3 8B).

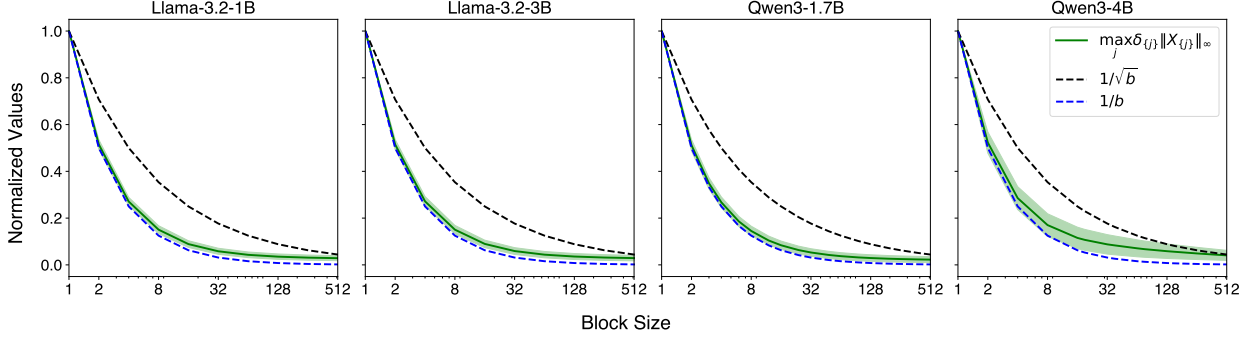


Figure 4: In **green**, we plot, for each block size  $b$ , the empirical mean and standard deviation of  $\max_j \delta_{j,j} \|X_{j,j}\|_\infty$ , normalized by  $\|X\|_\infty$ . Statistics are computed over all down projection layers using 10K tokens sampled from the WikiText2 dataset [19]. For reference, the  $1/\sqrt{b}$  trend is shown in **black** and the  $1/b$  trend is shown in **blue**.

Llama3 and Qwen3 models that we evaluated, the observed values of  $\max_j \delta_{j,j} \|X_{j,j}\|_\infty / \|X\|_\infty$  fall well-below this threshold for a wide range of block sizes. Thus, in this regime, Proposition 3.3 predicts a reduction in the range of the rotated vectors. To complement this analytically, we provide a probabilistic analysis of how outlier suppression evolves with block size via the following proposition.

**Proposition 3.5** (Probabilistic Evolution of Post-Rotation Outliers). *Let  $\tilde{R} = I_n \otimes R$  be a block rotation, where  $R \in \mathbb{R}^{b \times b}$  is a normalized Hadamard matrix and  $\tilde{R} \in \mathbb{R}^{d \times d}$  with  $d = nb$ . Given  $Y = (Y_1, \dots, Y_d) \in \mathbb{R}^d$ , let  $S = (S_1, \dots, S_d)$  be a random vector with i.i.d. Rademacher entries  $S_i \sim \text{Rad}(\pm 1)$ . Define activation vector  $X \in \mathbb{R}^d$  coordinate-wise as  $X_i = S_i Y_i$  for  $i \in [d]$ . Then, conditional on  $Y$ ,*

$$\|X \tilde{R}\|_\infty \leq \sqrt{\frac{2}{b} \log\left(\frac{2d}{\varepsilon}\right) \|X\|_2^2} \quad (3)$$

with probability at least  $1 - \varepsilon$ .

From Equation 3, we can reason about the expected behavior of post-rotation outliers beyond the adversarial worst case. Under mild assumptions, which we test in Appendix D.4, the expected worst-case post-rotation outlier decreases with block size  $b$  with high probability. This reveals an explicit trade-off: larger blocks decrease maximum post-rotation outliers with high probability but increase minimum computational requirements, as summarized in Remark 3.2. Moreover, Proposition 3.5 offers a complementary geometric perspective. In particular, outlier suppression is also probabilistically limited by mass concentration (see Remark D.5).

## 4 MixQuant: A Framework for Equalizing Permutation-Equivariant Regions

Both our deterministic and probabilistic bounds make clear that the worst-case outlier, and therefore the worst-case quantization error, is governed by blocks with the largest mass. In particular, the bound in Equation 2 implies

$$\|X \tilde{R}\|_\infty \leq \max_j \delta_{j,j} \sqrt{b} \|X_{j,j}\|_\infty \propto \max_j \|X_{j,j}\|_1,$$

where the proportionality follows from the definition  $\delta_{j,j} = \|X_{j,j}\|_1 / (b \|X_{j,j}\|_\infty)$ . Thus, for a fixed block size  $b$ , the tightest bound is achieved by minimizing  $\max_j \|X_{j,j}\|_1$ , which corresponds to balancing the per-block  $\ell_1$  norms. Intuitively, for a fixed  $X$ , block rotations are most effective when large-magnitude coordinates are distributed evenly across blocks rather than concentrated within a subset of them. This motivates our core design principle: permute activation coordinates to minimize the maximum per-block  $\ell_1$  norm before applying block rotations.

**MixQuant Overview.** MixQuant operationalizes the above design principle by equalizing blockwise activation mass prior to rotation using the pipeline illustrated in Figure 2. Given pre-trained weights and activations, MixQuant first computes a permutation to redistribute activation mass. To this end, we propose a permutation algorithm, termed mass diffusion (MassDiff), that greedily minimizes the expected maximum per-block  $\ell_1$  norm over a calibration dataset (pseudocode in Algorithm 1). While we focus on MassDiff in this work, the MixQuant framework naturally admits alternative permutation strategies, which we explore in Appendix C. The permuted activations are then block-rotated and rounded, after which error correction algorithms such as GPTQ [23] or Qronos [24] can be applied to the weights

---

**Algorithm 1** Mass Diffusion (MassDiff) Algorithm

---

**Require:** Calibration dataset  $\mathcal{D} = \{X^{(1)}, \dots, X^{(m)}\}$ , block size  $b$ , number of blocks  $n = d/b$

$\mathcal{J} \leftarrow \{1, \dots, n\}$   $\triangleright$  Initialize the set of valid blocks

$\mathcal{B}_j \leftarrow \emptyset$  for all  $j \in \mathcal{J}$   $\triangleright$  Initialize the set of indices for each valid block

$\mathcal{I} \leftarrow \text{argsort}_i(\frac{1}{m} \sum_{k=1}^m |X_i^{(k)}|)$   $\triangleright$  Initialize the set of coordinate indices sorted by descending average magnitude

**for**  $i \in \mathcal{I}$  **do**

$j^* = \arg \min_{j \in \mathcal{J}} \frac{1}{m} \sum_{k=1}^m \|X_{\mathcal{B}_j}^{(k)}\|_1 + |X_i^{(k)}|$   $\triangleright$  Find the set to minimize the average maximum per-block  $\ell_1$  norm

$\mathcal{B}_{j^*} \leftarrow \mathcal{B}_{j^*} \cup \{i\}$   $\triangleright$  Update the set of indices for the selected block

**if**  $|\mathcal{B}_{j^*}| = b$  **then**

$\mathcal{J} \leftarrow \mathcal{J} \setminus \{j^*\}$   $\triangleright$  Remove  $j^*$  from the set of valid blocks if the block is full

**end if**

**end for**

**Return**  $[\mathcal{B}_1, \dots, \mathcal{B}_n]$   $\triangleright$  Concatenate the sets to return the permutation

---

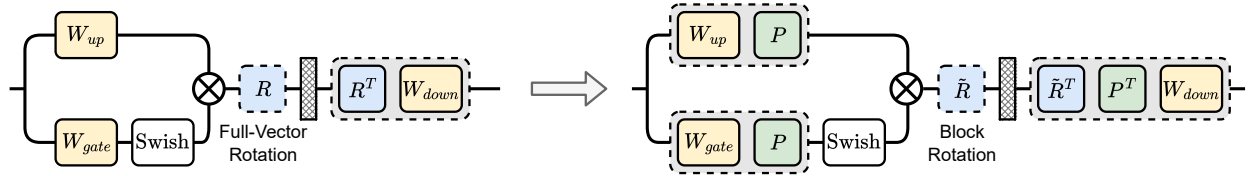


Figure 5: MixQuant replaces full-vector rotation  $R$  with permutation  $P$  and block rotation  $\tilde{R}$ , as shown here for the feedforward network in the standard transformer architecture. Importantly, this subgraph is a permutation-equivariant region (formally defined in Definition 4.1) but it is not rotation-equivariant due to the Swish activation function. So,  $P$  can be merged into the surrounding weights prior to inference, while  $R$  and  $\tilde{R}$  remain as online rotations.

without modification. Importantly, equalization is performed once on the full-precision model and the resulting permutations are fused into surrounding layers before deployment, as described next.

**Permutation Equivariance in Neural Networks.** At first glance, introducing permutations may appear to alter the network computation. However, permutations can be introduced in a way that preserves functional behavior without introducing overhead. To formalize this idea, we define permutation-equivariant regions as a class of network subgraphs within which permutations can be freely commuted and absorbed into surrounding linear layers before deployment.

**Definition 4.1** (Permutation-Equivariant Region). *A permutation-equivariant region is a contiguous subgraph of a neural network of the form  $\Phi := f_n \circ \dots \circ f_1$  whose map  $\Phi : (\mathbb{R}^d)^m \rightarrow (\mathbb{R}^d)^{m'}$  satisfies the following property: for any activation vectors  $X^{(1)}, \dots, X^{(m)} \in \mathbb{R}^d$  and any permutation matrix  $P \in \mathbb{R}^{d \times d}$  acting on the feature dimension, if*

$$\Phi(X^{(1)}, \dots, X^{(m)}) = (Y^{(1)}, \dots, Y^{(m')})$$

then

$$\Phi(X^{(1)}P, \dots, X^{(m)}P) = (Y^{(1)}P, \dots, Y^{(m')}P).$$

Note that elementwise operations such as Swish or ReLU activation functions are equivariant to permutations along the feature dimension. Permutation-equivariant regions are therefore prevalent in neural network architectures, thus enabling one to introduce permutations without modifying the execution graph, as formalized in the following remark.

**Remark 4.2** (Merging Permutations). In identifying permutation-equivariant regions in a neural network, one can freely commute permutations through the corresponding subgraph to be absorbed into surrounding linear layers. For example, consider activation vector  $X \in \mathbb{R}^d$ , permutation matrix  $P \in \mathbb{R}^{d \times d}$ , and weight matrices  $W_1, W_2 \in \mathbb{R}^{d \times d}$ . Let permutation-equivariant region  $\Phi$  be unary (*i.e.*,  $m = m' = 1$ ) such that  $\Phi : \mathbb{R}^d \rightarrow \mathbb{R}^d$ . Then,

$$\Phi(XW_1)W_2 = \Phi(XW_1P)P^TW_2 = \Phi(X\tilde{W}_1)\tilde{W}_2,$$

where  $\tilde{W}_1 = W_1P$  and  $\tilde{W}_2 = P^TW_2$ . Therefore, for  $g_i(X) = XW_i$ , regions of the form  $\Psi := g_2 \circ \Phi \circ g_1$  are functionally equivalent under permutations of the feature dimension. This property enables MixQuant to equalize activation mass across blocks with permutations that can be merged into surrounding weights before deployment, therefore leaving the graph unaltered and incurring no additional inference-time overhead. Figure 5 illustrates this process for the feedforward network of a standard transformer block, where the Swish activation function and elementwise multiplication form a multi-input, single-output region within which permutation matrix  $P$  can be commuted.

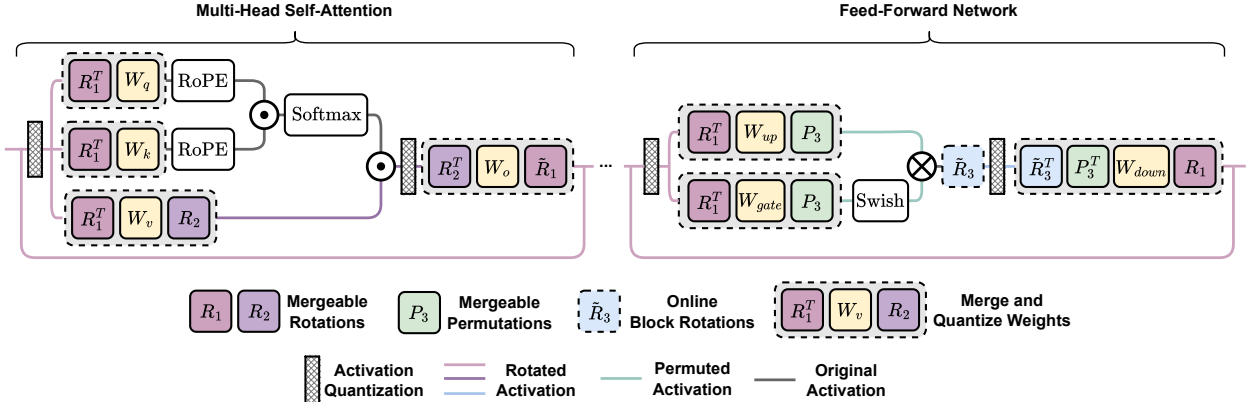


Figure 6: We illustrate our quantization graph architecture for a standard transformer block, merging rotations and permutations wherever possible and quantizing the weights and activations for all linear layers.

## 5 Experimental Results

The core contribution of this work is MixQuant—our principled framework for improving the outlier suppression capabilities of block rotations by equalizing activation mass across blocks within permutation-equivariant regions of a compute graph. We therefore design our experiments to isolate the impact of permutations on preserving the accuracy of block-rotated LLMs quantized to narrow data formats, and to empirically validate our theoretical analysis.

**Models & Datasets.** We conduct experiments on Llama3 [25] and Qwen3 [18] models. We use the implementations and instruction fine-tuned checkpoints made publicly available via Huggingface [26] without modification. We construct our calibration dataset using 128 random sequences of 2048 tokens sampled from the WikiText2 [19] training dataset, and evaluate perplexity on the corresponding test split. While perplexity serves as a standard proxy for generative quality, it does not directly reflect downstream reasoning performance; we complement it with an analysis of zero-shot accuracy to assess generalization. Specifically, we use LightEval [27] to evaluate five reasoning tasks: ARC (challenge and easy) [28], HellaSwag [29], PIQA [30], and Winogrande [31]. We note that comprehensive LLM evaluation remains an open problem, and we leave deeper analyses for future work.

**Implementation Details.** To describe our implementations, we decouple the *quantization graph* from the *quantization pipeline*. The former specifies where permutations and rotations are inserted into the compute graph, while the latter defines how different methods are composed throughout our experiments. Figure 6 illustrates the quantization graph architecture primarily considered in our experiments. Rotations are merged into linear layers when possible ( $R_1$  and  $R_2$ ) and online rotations are only present at the inputs to the down projection layer in the feedforward network ( $\tilde{R}_3$ ). MixQuant is defined at the pipeline level as a framework for equalizing permutation-equivariant regions; concrete methods correspond to different compositions of permutation, rotation, and rounding algorithms within the pipeline visualized in Figure 2. We primarily evaluate two MixQuant compositions. **MixQuant\*** composes our MassDiff permutation with full-vector Hadamard rotations at  $R_1$  and  $R_2$ , block Hadamard rotations at  $\tilde{R}_3$ , and Qronos rounding. **MixQuant<sup>†</sup>** uses the same permutation and block rotation at  $\tilde{R}_3$ , but learns full-vector rotations  $R_1$  and  $R_2$  via Cayley optimization [9] before rounding to nearest (RTN). For all MixQuant variants, we apply block rotations only at  $\tilde{R}_3$  and equalize only those regions in the graph;  $R_1$  and  $R_2$  are full-vector and are not equalized. We provide hyperparameters and additional implementation details in Appendix B. Furthermore, we perform a series of ablation studies to assess the impact of key design choices in Appendix C, including the permutation method, rotation merging strategy, and pipeline composition. We implement all variants of MixQuant in PyTorch with the Brevitas quantization library [32]. We quantize all models using a single AMD Instinct MI210 GPU<sup>3</sup> with 64GB of memory.

**Baseline Details.** We compare MixQuant against MR-GPTQ [3] and BRQ [2], which are both recent methods that apply block rotations and perform rounding using GPTQ. To ensure a controlled comparison, we evaluate MR-GPTQ and BRQ using the same quantization graph architecture illustrated in Figure 6, merging rotations into linear layers when possible. MR-GPTQ and BRQ are therefore equivalent within our experiment design: both correspond to applying merged block rotations at  $R_1$  and  $R_2$ , and online block rotations at  $\tilde{R}_3$  with an identity permutation  $P_3 = I_d$ , followed by GPTQ rounding. We study the unfused, fully online rotation architecture originally proposed in [3] separately in an

<sup>3</sup>AMD, AMD Instinct, and combinations thereof are trademarks of Advanced Micro Devices, Inc.

Table 2: We present the WikiText2 perplexity of Llama3 models quantized to INT4, comparing block rotations with and without MixQuant across block sizes. We provide full-vector rotations for reference, which is equivalent to QuaRot. All results use Qronos for error correction; additional results with RTN and GPTQ are provided in Table 6. Reference BF16 baselines are provided in Table 3.

		16	32	64	128	256	512	1024	2048	Full
<b>1B</b>	No Permute	35.8	25.4	23.5	20.4	18.9	17.5	16.6	16.4	16.1
	MixQuant	18.2	16.9	16.6	<b>15.9</b>	<b>15.9</b>	16.1	16.1	16.1	16.1
<b>3B</b>	No Permute	18.9	15.6	14.4	14.4	14.0	13.8	13.2	13.4	12.6
	MixQuant	14.2	13.3	12.8	12.6	<b>12.4</b>	12.6	12.6	12.6	12.6
<b>8B</b>	No Permute	32.0	12.8	9.5	8.8	8.4	8.2	8.2	8.1	<b>7.9</b>
	MixQuant	9.5	8.5	8.1	8.0	<b>7.9</b>	<b>7.9</b>	<b>7.9</b>	<b>7.9</b>	<b>7.9</b>

ablation (Appendix C). In addition to MR-GPTQ/BRQ, we introduce two variants that isolate the effect of the rounding stage: MR-RTN and MR-Qronos, which replace GPTQ with RTN and Qronos, respectively, while applying the same block rotations. We also evaluate BRQ-Spin, which learns block rotations at  $R_1, R_2 \in \mathbb{R}^{b \times b}$  via Cayley optimization before rounding with GPTQ. We provide additional implementation details in Appendix B.

**Evaluation of Block Size.** We first evaluate the extent to which our theoretical analysis is predictive by measuring the impact of block size on model quality within the Llama3 model family. Table 2 reports WikiText2 perplexity comparing block rotations with and without permutations when quantizing weights and activations to 4-bit integers (INT4). We use Qronos as our rounding algorithm here, and report additional results with RTN and GPTQ in Table 6.

Three clear trends emerge. First, in the absence of permutations, model quality generally improves as block size increases, with perplexity approaching that of full-vector rotations (equivalent to QuaRot with Qronos). This behavior is consistent with Equation 3, which predicts post-rotation outliers are reduced as  $b \rightarrow d$  with diminishing returns. Second, and more importantly, MixQuant consistently improves perplexity across all models and block sizes, with particularly large gains at small block sizes. Even with block sizes of 16, MixQuant recovers most of the accuracy gap to full-vector rotations, and often completely closes the gap with block sizes of 128 or greater, demonstrating the effectiveness of permutations in mitigating the limitations of block rotations as identified in Proposition 3.3. Finally, we observe a scaling trend with model size: with a block size of 16, MixQuant recovers approximately 90%, 88%, and 83% of full-vector rotation accuracy for Llama3 1B, 3B, and 8B, respectively. This decreasing recovery is expected as larger models tend to have higher activation kurtosis [20], which requires larger block sizes to maintain accuracy.

**Comparisons with Block Rotation Baselines.** Table 3 reports WikiText2 perplexity and average zero-shot accuracy for Llama3 and Qwen3 models across multiple data formats. All methods share the same quantization graph and differ only in their pipeline composition. Following the MR-GPTQ and BRQ proposals, all block rotations in this comparison use a fixed block size of 32.

Our results show that INT4 is a stringent stress test for block rotations. MR-RTN and MR-GPTQ/BRQ frequently exhibit severe degradation in this regime, even with gradient-based rotation optimization (BRQ-Spin). Replacing GPTQ with Qronos substantially improves MR-style baselines, but remains far from the full-precision baseline. In comparison, MixQuant consistently improves perplexity and on average maintains over 91% of the full-precision zero-shot accuracy across both model families, with and without gradients. These trends support our theoretical analysis: while improved rounding can further reduce quantization error, MixQuant directly addresses the limitations of block rotations identified in Section 3.2. Interestingly, we observe that MixQuant<sup>†</sup> sometimes achieves lower perplexity than the full-precision baseline (*e.g.*, Qwen3 1.7B and 4B). In most cases, these gains are accompanied by modest reductions in zero-shot accuracy, suggesting mild overfitting to the calibration dataset. We note that this behavior is consistent with prior observations in which fine-tuning from a checkpoint can improve test accuracy despite quantization in the loop [33, 34].

The interaction between quantization pipeline composition and target data format yields additional insights. MR-GPTQ and BRQ were primarily proposed for and evaluated on microscaling (MX) formats, which inherently mitigate outliers via group-wise scaling. In contrast, INT4 and FP4 rely on per-channel scaling and are therefore more sensitive to outliers. Accordingly, consistent with the results from [3] and [2], we observe that MR-style baselines perform substantially better on MXFP4 than on FP4 or INT4. Nevertheless, even for MXFP4, MixQuant<sup>†</sup> consistently yields the best perplexity across both model families, and on average maintains 95% of the full-precision zero-shot accuracy. Interestingly, while FP4 is generally more forgiving than INT4 for MR-style pipelines, we highlight that MixQuant consistently performs better on INT4 than on FP4, with MixQuant<sup>†</sup> consistently improving over MixQuant\* across all formats.

Table 3: We report WikiText2 perplexity and average zero-shot accuracy for Llama3 and Qwen3 models quantized to various data formats using different pipeline compositions, all instantiated within the same graph architecture visualized in Figure 6. All variants of MR-GPTQ and BRQ apply block rotations without permutation, while MixQuant compositions incorporate permutation-based equalization prior to rotation.

Format	Methods	Llama3						Qwen3					
		WikiText2 (↓)			0-shot (↑)			WikiText2 (↓)			0-shot (↑)		
		1B	3B	8B	1B	3B	8B	1.7B	4B	8B	1.7B	4B	8B
BF16	-	11.8	9.8	6.5	51.8	59.8	66.0	15.2	12.2	8.6	48.4	50.9	53.5
INT4	MR-RTN	3e3	1e4	9e3	34.9	34.8	34.7	9e2	8e2	1e2	35.2	34.8	36.2
	MR-GPTQ / BRQ	2e3	6e3	7e3	35.1	34.9	35.1	9e2	2e2	79.5	35.3	36.3	36.5
	MR-Qronos	41.8	84.5	1e2	38.7	36.9	35.5	41.8	35.8	24.3	38.1	41.1	41.3
	BRQ-Spin	1e3	5e3	5e3	34.6	34.4	34.8	5e2	2e2	56.2	35.4	35.6	36.3
	MixQuant*	16.9	13.3	8.5	47.7	54.2	60.3	18.9	14.9	10.8	44.0	47.0	49.9
	MixQuant <sup>†</sup>	<b>15.9</b>	<b>10.9</b>	<b>8.4</b>	46.8	<b>56.1</b>	<b>60.9</b>	<b>13.6</b>	<b>11.1</b>	<b>9.5</b>	<b>45.8</b>	46.7	<b>50.7</b>
FP4	MR-RTN	70.0	40.5	26.6	39.2	44.5	46.2	93.0	4e2	1e2	37.3	35.6	38.5
	MR-GPTQ / BRQ	43.2	27.0	18.9	42.6	47.0	50.7	60.0	2e2	93.0	38.0	37.5	39.2
	MR-Qronos	23.9	15.9	11.6	44.4	<b>51.9</b>	53.5	29.2	72.5	26.2	40.8	37.8	42.5
	BRQ-Spin	51.2	31.1	20.4	41.4	47.0	48.8	54.5	1e2	39.2	39.2	37.5	41.1
	MixQuant*	21.0	16.6	10.6	44.2	51.6	54.9	21.4	16.6	12.0	42.4	<b>45.5</b>	47.7
	MixQuant <sup>†</sup>	<b>18.0</b>	<b>12.8</b>	<b>9.8</b>	<b>46.1</b>	51.5	<b>55.6</b>	<b>15.6</b>	<b>12.4</b>	<b>9.8</b>	<b>43.2</b>	45.0	<b>49.6</b>
MXFP4	MR-RTN	18.5	15.2	8.2	47.8	52.1	61.5	23.1	23.5	11.2	43.0	47.8	50.3
	MR-GPTQ / BRQ	14.2	11.2	7.4	50.3	57.5	63.4	16.9	14.9	9.6	<b>46.8</b>	48.7	52.8
	MR-Qronos	14.0	11.6	7.4	<b>51.0</b>	<b>57.6</b>	62.4	16.9	14.9	9.6	45.5	48.6	51.4
	BRQ-Spin	14.9	13.2	7.8	48.5	53.6	<b>63.8</b>	19.1	12.6	9.6	44.9	49.0	51.6
	MixQuant*	14.2	11.4	7.4	48.3	57.5	63.1	17.1	14.0	9.9	46.0	48.7	50.6
	MixQuant <sup>†</sup>	<b>13.2</b>	<b>9.6</b>	<b>7.2</b>	49.1	57.2	63.0	<b>11.8</b>	<b>9.3</b>	<b>7.8</b>	46.7	<b>50.5</b>	<b>54.2</b>

## 6 Discussion & Conclusions

We present the first systematic, non-asymptotic analysis of outlier suppression with block Hadamard rotations. Our analysis yields sufficient conditions under which Hadamard rotations suppress outliers, and reveals that the effectiveness of block Hadamard rotations is fundamentally limited by the activation block with the largest mass. Guided by these insights, we design MixQuant to equalize blockwise activation mass prior to rotation. Our experimental results closely align with our analysis: MixQuant consistently improves model quality with block Hadamard rotations across block sizes, data formats, and model families, which validates our central claim that equalizing mass across blocks mitigates the limitations we identified. Moreover, MixQuant outperforms existing block rotation baselines, namely MR-GPTQ and BRQ variants. Finally, from a systems perspective, the overhead introduced by MixQuant is negligible; MassDiff calibrates permutations in under two minutes for Llama3 8B, and the resulting matrices are fully merged into the graph before deployment to avoid adding inference overhead.

**Ablations.** We perform a series of ablation studies to assess the impact of key design choices in Appendix C, including the permutation method, rotation merging strategy, and pipeline composition. Across models, MassDiff consistently outperforms alternative permutation methods (Table 5), reinforcing the importance of equalizing activation mass prior to rounding to improve outlier suppression. We also find that rotation merging and pipeline composition exhibit non-trivial interactions (Tables 6 and 7). We leave a more systematic exploration of these interactions to future work.

**Limitations.** Our analysis is based on non-asymptotic bounds characterizing worst-case behavior for activation outlier suppression with block Hadamard rotations. While this perspective is useful for identifying fundamental limitations, it does not aim to predict performance for all models, datasets, or data formats. In practice, substantial variation exists within these bounds, depending on the complex interaction between models, datasets, and quantization schemes, among other components. This limitation is most clearly reflected in MX formats such as MXFP4, which inherently mitigate outliers via group-wise scaling; in this regime, outlier suppression with rotations is less critical, and the performance gap between MixQuant and MR-style baselines narrows. These observations highlight that the benefits of permutation-based equalization are most pronounced in settings where outliers materially impact quantization error. Finally, our theoretical analysis does not explicitly account for weight outlier suppression or alternative rotation structures, such as the Givens matrices studied in [12]. We leave such extensions for future work.

**Reproducibility Statement.** We integrate MixQuant into the open-source Brevitas quantization library. Our code and instructions on how to reproduce experiments, including hyperparameters and random seeds, can be found here: [https://github.com/i-colbert/brevitas/tree/mixquant/src/brevitas\\_examples/papers/mixquant](https://github.com/i-colbert/brevitas/tree/mixquant/src/brevitas_examples/papers/mixquant).

## Acknowledgements

We would like to thank Michaela Blott, Gabor Sines, Ralph Wittig, Syed Naim, Yonas Bedasso, and Max Keihn from AMD for their support.

## References

- [1] S. Ashkboos, A. Mohtashami, M. L. Croci, B. Li, P. Cameron, M. Jaggi, D. Alistarh, T. Hoefer, and J. Hensman, “QuaRot: Outlier-free 4-bit inference in rotated LLMs,” 2024.
- [2] Y. Shao, P. Wang, Y. Chen, C. Xu, Z. Wei, and J. Cheng, “Block rotation is all you need for MXFP4 quantization,” *arXiv preprint arXiv:2511.04214*, 2025.
- [3] V. Egiazarian *et al.*, “Bridging the gap between promise and performance for microscaling FP4 quantization,” *arXiv preprint arXiv:2509.23202*, 2025.
- [4] G. Xiao, J. Lin, M. Seznec, H. Wu, J. Demouth, and S. Han, “Smoothquant: accurate and efficient post-training quantization for large language models,” in *Proceedings of the 40th International Conference on Machine Learning*, ser. ICML’23. JMLR.org, 2023.
- [5] J. Lin, J. Tang, H. Tang, S. Yang, G. Xiao, and S. Han, “AWQ: Activation-aware weight quantization for on-device llm compression and acceleration,” *GetMobile: Mobile Comp. and Comm.*, vol. 28, no. 4, p. 12–17, Jan. 2025.
- [6] J. Chee, Y. Cai, V. Kuleshov, and C. D. Sa, “QuIP: 2-bit quantization of large language models with guarantees,” in *Thirty-seventh Conference on Neural Information Processing Systems*, 2023.
- [7] H. Adepu, Z. Zeng, L. Zhang, and V. Singh, “FrameQuant: Flexible low-bit quantization for transformers,” *arXiv preprint arXiv:2403.06082*, 2024.
- [8] G. Franco, P. Monteagudo-Lago, I. Colbert, N. Fraser, and M. Blott, “Improving quantization with post-training model expansion,” 2025.
- [9] Z. Liu, C. Zhao, I. Fedorov, B. Soran, D. Choudhary, R. Krishnamoorthi, V. Chandra, Y. Tian, and T. Blankevoort, “SpinQuant: LLM quantization with learned rotations,” in *The Thirteenth International Conference on Learning Representations*, 2025.
- [10] X. Hu, Y. Cheng, D. Yang, Z. Xu, Z. Yuan, J. Yu, C. Xu, Z. Jiang, and S. Zhou, “OSTQuant: Refining large language model quantization with orthogonal and scaling transformations for better distribution fitting,” 2025.
- [11] Y. Sun *et al.*, “FlatQuant: Flatness matters for llm quantization,” *arXiv preprint arXiv:2410.09426*, 2024.
- [12] B. Xu, Z. Dong, O. Elachqar, and Y. Shang, “ButterflyQuant: Ultra-low-bit llm quantization through learnable orthogonal butterfly transforms,” *arXiv preprint arXiv:2509.09679*, 2025.
- [13] H. Lin, H. Xu, Y. Wu, J. Cui, Y. Zhang, L. Mou, L. Song, Z. Sun, and Y. Wei, “DuQuant: Distributing outliers via dual transformation makes stronger quantized llms,” *Advances in Neural Information Processing Systems*, vol. 37, pp. 87766–87800, 2024.
- [14] A. Gholami, S. Kim, Z. Dong, Z. Yao, M. W. Mahoney, and K. Keutzer, “A survey of quantization methods for efficient neural network inference,” in *Low-power computer vision*. Chapman and Hall/CRC, 2022, pp. 291–326.
- [15] A. Zhang, N. Wang, Y. Deng, X. Li, Z. Yang, and P. Yin, “MagR: Weight magnitude reduction for enhancing post-training quantization,” *Advances in neural information processing systems*, vol. 37, pp. 85109–85130, 2024.
- [16] H. Zhang, S. Zhang, I. Colbert, and R. Saab, “Provable post-training quantization: Theoretical analysis of OPTQ and Qronos,” *arXiv preprint arXiv:2508.04853*, 2025.
- [17] A. Grattafiori *et al.*, “The llama 3 herd of models,” 2024.
- [18] A. Yang *et al.*, “Qwen3 technical report,” 2025.
- [19] S. Merity, C. Xiong, J. Bradbury, and R. Socher, “Pointer sentinel mixture models,” *arXiv preprint arXiv:1609.07843*, 2016.
- [20] S. Li, X. Ning, L. Wang, T. Liu, X. Shi, S. Yan, G. Dai, H. Yang, and Y. Wang, “Evaluating quantized large language models,” in *Proceedings of the 41st International Conference on Machine Learning*, 2024, pp. 28480–28524.

- [21] B. Fino and R. Algazi, “Unified matrix treatment of the fast walsh-hadamard transform,” *IEEE Transactions on Computers*, vol. C-25, no. 11, pp. 1142–1146, 1976.
- [22] T. Dao, “Fast hadamard transform in CUDA, with a PyTorch interface,” 2023.
- [23] E. Frantar, S. Ashkboos, T. Hoefler, and D. Alistarh, “GPTQ: Accurate post-training quantization for generative pre-trained transformers,” *arXiv preprint arXiv:2210.17323*, 2022.
- [24] S. Zhang, H. Zhang, I. Colbert, and R. Saab, “Qronos: Correcting the past by shaping the future... in post-training quantization,” *arXiv preprint arXiv:2505.11695*, 2025.
- [25] H. Touvron *et al.*, “Llama 2: Open foundation and fine-tuned chat models,” *arXiv preprint arXiv:2307.09288*, 2023.
- [26] T. Wolf *et al.*, “Transformers: State-of-the-art natural language processing,” in *Proceedings of the 2020 Conference on Empirical Methods in Natural Language Processing: System Demonstrations*. Online: Association for Computational Linguistics, Oct. 2020, pp. 38–45.
- [27] N. Habib, C. Fourrier, H. Kydlíček, T. Wolf, and L. Tunstall, “LightEval: A lightweight framework for llm evaluation,” 2023.
- [28] P. Clark, I. Cowhey, O. Etzioni, T. Khot, A. Sabharwal, C. Schoenick, and O. Tafjord, “Think you have solved question answering? Try ARC, the AI2 reasoning challenge,” *arXiv preprint arXiv:1803.05457*, 2018.
- [29] R. Zellers, A. Holtzman, Y. Bisk, A. Farhadi, and Y. Choi, “HellaSwag: Can a machine really finish your sentence?” *arXiv preprint arXiv:1905.07830*, 2019.
- [30] Y. Bisk, R. Zellers, J. Gao, Y. Choi *et al.*, “PIQA: Reasoning about physical commonsense in natural language,” in *Proceedings of the AAAI conference on artificial intelligence*, vol. 34, no. 05, 2020, pp. 7432–7439.
- [31] K. Sakaguchi, R. L. Bras, C. Bhagavatula, and Y. Choi, “Winogrande: An adversarial winograd schema challenge at scale,” *Communications of the ACM*, vol. 64, no. 9, pp. 99–106, 2021.
- [32] G. Franco, A. Pappalardo, and N. J. Fraser, “Xilinx/brevitas,” 2025.
- [33] I. Colbert, A. Pappalardo, J. Petri-Koenig, and Y. Umuroglu, “A2Q+: Improving accumulator-aware weight quantization,” *arXiv preprint arXiv:2401.10432*, 2024.
- [34] Z. Liu *et al.*, “ParetoQ: Scaling laws in extremely low-bit LLM quantization,” *arXiv preprint arXiv:2502.02631*, 2025.
- [35] X. Zhang, I. Colbert, and S. Das, “Learning low-precision structured subnetworks using joint layerwise channel pruning and uniform quantization,” *Applied Sciences*, vol. 12, no. 15, p. 7829, 2022.
- [36] Open Compute Project Foundation, “OCP microscaling formats (MX) specification v1.0,” Open Compute Project, Tech. Rep., 2024, accessed: 2025-07-15.
- [37] I. Colbert, G. Franco, F. Grob, J. Zhang, and R. Saab, “Accumulator-aware post-training quantization for large language models,” *Transactions on Machine Learning Research*, 2025.
- [38] Y. Bengio, N. Léonard, and A. Courville, “Estimating or propagating gradients through stochastic neurons for conditional computation,” *arXiv preprint arXiv:1308.3432*, 2013.
- [39] O. Hölder, “Ueber einen mittelwerthabsatz,” *Nachrichten von der Königl. Gesellschaft der Wissenschaften und der Georg-Augusts-Universität zu Göttingen*, vol. 1889, pp. 38–47, 1889.
- [40] R. Vershynin, *High-dimensional probability: An introduction with applications in data science*. Cambridge university press, 2018, vol. 47.

## A Optimized Non-Power-of-2 Hadamard Architecture

Let  $X \in \mathbb{R}^d$  be an activation vector and  $R \in \mathbb{R}^{d \times d}$  be a Hadamard matrix, with  $d \geq 4$ . If the dimension  $d$  is a power of 2, the rotation of  $X$  by  $R$  can be fully decomposed into butterfly stages, resulting in  $\mathcal{O}(d \log d)$  add/subtract operations. If  $d$  is not a power of 2, it can be factored into a power of 2 and a non-power-of-2 component as  $d = kt$ , where  $t$  is the largest non-power-of-2 factor of  $d$  and  $k$  is the power-of-2 remainder. Because the matrix  $R$  is constructed from  $k' = \log(k) - 2$  recursive applications of a  $4t$ -dimensional base matrix, the overall computation naturally splits into two parts: (1)  $k'$  radix-2 butterfly stages, followed by (2)  $2^{k'}$  instances of  $4t$ -dimensional rotations.

The  $4t$ -dimensional rotations themselves can be further optimized by first computing all sums and differences over every group of four adjacent inputs, and then performing a final stage that adds or subtracts  $4t$  groups of  $t$  elements according to a sign pattern determined by the definition of the  $4t$ -dimensional Hadamard matrix. Figure 7 illustrates this rotation structure for an activation vector in the Llama3 8B model with dimension 14334. This dimension factorizes as  $512 \times 28$ , resulting in 9 radix-2 butterfly stages and 512 independent 28-dimensional rotations. Each 28-dimensional rotation is further decomposed into three stages: the first two stages compute seven groups of four-input additions and subtractions, and the final stage performs 28 groups of seven-input add and subtract operations.

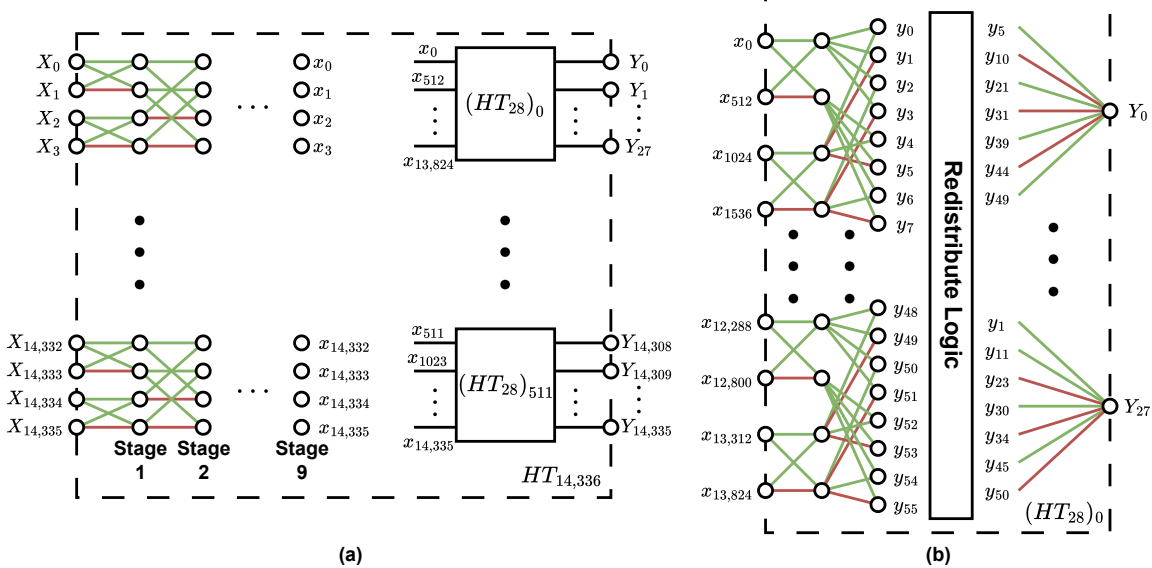


Figure 7: Structure of (a) 14336-dimensional Hadamard rotation and (b) 28-dimensional sub-rotation  $(HT_{28})_0$ . All lines marked in green are additions and the ones marked in red are subtractions.

Our proposed optimization reduces the number of add/subtract operations of a  $d$ -dimensional rotation from  $\mathcal{O}(d(k' + 4t - 1))$  to  $\mathcal{O}(d(k' + t + 2))$ , equivalently  $\mathcal{O}(dt + d \log k)$ . Due to the nature of the optimization, this provides the largest gains when  $k'$  is small and  $t$  is large. In particular, for fixed  $k'$  and as  $t \rightarrow \infty$ , the reduction asymptotically yields a  $4\times$  reduction in operation count. Table 4 reports the number of operations required for online rotations in non-power-of-2 dimensions found in Llama3 and Qwen3 models, comparing our reduction to existing techniques. Overall, our approach reduces the total number of operations by orders of magnitude relative to dense multiplication, and  $1.4 - 2.9\times$  improvement over existing butterfly decomposition-based implementations [22].

Table 4: We report the number of operations required to rotate the input to the down projection layer in various LLMs with different methods, as well as the reduction in operations (in parentheses).

Model	$d$	$2^{k'} \times 4t$	Matmul	Butterfly + Matmul	Ours
Llama3-8B	14336	$2^9 \times 28$	205.51M (796.4 $\times$ )	516.10K (2.0 $\times$ )	258.05K
Qwen3-0.6B	3072	$2^8 \times 12$	9.43M (236.3 $\times$ )	58.37K (1.5 $\times$ )	39.94K
Qwen3-1.7B	6144	$2^9 \times 12$	37.74M (438.8 $\times$ )	122.88K (1.4 $\times$ )	86.02K
Qwen3-4B	9728	$2^7 \times 76$	94.62M (347.4 $\times$ )	797.70K (2.9 $\times$ )	272.38K
Qwen3-8B	12288	$2^{10} \times 12$	150.98M (819.1 $\times$ )	258.05K (1.4 $\times$ )	184.32K

## B Additional Implementation Details

**INT4 Quantization.** We use the  $q$ -bit integer quantizer defined as

$$\mathcal{Q}(X) = s \cdot \text{clip} \left( \left\lfloor \frac{X}{s} \right\rfloor - z, \min \mathcal{A}, \max \mathcal{A} \right) + z, \quad (4)$$

where  $s$  is the quantization step size (or scaling factor),  $z$  is the zero-point, and  $\lfloor \cdot \rfloor$  is the round-to-nearest (RTN) operator [35, 14]. We quantize weights using the standard symmetric weight quantizer, where zero point  $z = 0$  and scaling factor  $s \in \mathbb{R}$  is optimized per-channel via linear search to minimize the mean squared error (MSE) loss between the full-precision and quantized weights, as is common practice [1, 3, 24]. Activations are quantized using the standard asymmetric activation quantizer, where zero point  $z = \min(X)/s$  and scaling factor  $s = (\max(X) - \min(X))/(2^q - 1)$  are dynamically defined per-token.

**(MX)FP4 Quantization.** We use the standard  $q$ -bit floating-point quantizer defined as

$$Q(X) := s \cdot \text{clip} \left( s' \left\lfloor \frac{X}{ss'} \right\rfloor ; \min \mathcal{A}, \max \mathcal{A} \right), \quad (5)$$

where  $\log s' = \max(\lfloor X/s \rfloor, 2^{e-1}) - m$  for target alphabet  $\mathcal{A}$  defined by  $m$  mantissa bits and  $e$  exponent bits. We adhere to the OCP specification [36], which defines  $e = 2$  and  $m = 1$  for FP4. We quantize weights and activations symmetrically with zero point  $z = 0$ . For FP4 weights, scaling factor  $s \in \mathbb{R}$  is optimized per-channel via linear search to minimize the MSE loss between the full-precision and quantized weights. For FP4 activations, scaling factor  $s = \|X\|_\infty/(2^{q-1} - 1)$  is defined dynamically per-token. For MXFP4 weights and activations, scaling factors are defined for each group of 32 elements and are rounded down to a power of 2. For example, the scaling factor for the  $j$ -th block in activation vector  $X$  is  $\log s_{\{j\}} = \log (\lfloor \|X_{\{j\}}\|_\infty/(2^{q-1} - 1) \rfloor)$ .

**Algorithm hyperparameters.** When applying GPTQ, the calibration set is constructed from 128 samples of 2048-token sequences drawn from the WikiText2 training set. We use the dampened covariance matrix  $\tilde{X}^T \tilde{X} + \lambda I_d$ , where  $\tilde{X}$  denotes the rotated and quantized activations and  $\lambda$  is 1% of the average diagonal of  $\tilde{X}^T \tilde{X}$ . We similarly use the dampened covariance matrix when applying Qronos, but choose  $\lambda$  to be based on the maximum singular value of the covariance matrix such that  $\lambda = \alpha \cdot \sigma_1$  with  $\alpha = 1e^{-3}$  as proposed by Zhang *et al.* [24]. For both GPTQ and Qronos, we quantize weights in descending order of the diagonal of  $\tilde{X}^T \tilde{X}$ , as it has become common practice [8, 37] and can provably improve error correction [16]. Note that, when composing MixQuant with GPTQ or Qronos,  $\tilde{X}$  is also permuted. When calibration permutations with MassDiff, we use only one sample of a 2048-token sequence randomly drawn from WikiText2; additional samples did not consistently yield additional benefit. When learning rotations, we draw 800 samples of 2048-token sequences for Cayley SGD, as proposed in [9]. In both cases, we still draw 128 samples for GPTQ or Qronos if error correction is applied. Unlike SpinQuant, which is applied after activation quantization but before weight quantization, we apply Cayley SGD for 100 epochs after both weights and activations have been quantized using the straight-through estimator [38]. All other hyperparameters (e.g., learning rate and batch size) remain unchanged from the original study by Liu *et al.* [9].

## C Ablations

We perform a series of ablation studies to assess the impact of key design choices, including the permutation method, rotation merging strategy, and pipeline composition. These experiments are intended to isolate the contribution of each component and to clarify how design decisions interact in practice.

**Permutations.** In Table 5, we compare alternative permutation strategies within a fixed MixQuant pipeline using Qronos rounding and block rotations with  $b = 32$  to quantize Llama3 and Qwen3 weights and activations to INT4. Random permutations are averaged over 5 seeds, “absmax” permutes coordinates in descending order of the maximum absolute value observed over the calibration sample, “zigzag” uses the strategy proposed in [13], and MassDiff is given by Algorithm 1. Across model families and sizes, MassDiff consistently outperforms these alternative permutation methods, highlighting the importance of redistributing coordinates prior to rounding to balance activation mass.

**Pipeline Composition.** Table 6 shows how rounding choices in Stage 2 interact with different transformation strategies in Stage 1 within the MixQuant pipeline visualized in Figure 2. From the graph visualized in Figure 6, “MassDiff + QuaRot” corresponds to a pipeline where full-precision weights and activations are first permuted via MassDiff at  $P_3$ , then full-vector Hadamard rotations are applied at  $R_1$  and  $R_2$  and an online block Hadamard rotation is applied at  $\tilde{R}_3$  to the permuted weights and activations. “MassDiff + SpinQuant” corresponds to a similar pipeline, but instead where full-vector rotations are learned at  $R_1$  and  $R_2$  via Cayley SGD. In these experiments, we use a block size of 32. Across

Table 5: We report WikiText2 perplexity and average zero-shot accuracy for different permutation methods evaluated under a fixed MixQuant pipeline using block rotations with  $b = 32$  and Qronos rounding, without learned rotations.

Method	Llama3						Qwen3					
	WikiText2 (↓)			0-shot (↑)			WikiText2 (↓)			0-shot (↑)		
1B	3B	8B	1B	3B	8B	1.7B	4B	8B	1.7B	4B	8B	
No Permute	25.6	15.6	12.9	43.8	48.6	35.4	43.2	16.6	12.6	38.2	46.7	48.0
Random	27.8	15.3	11.9	42.8	51.1	38.6	37.0	16.3	12.6	39.0	46.6	47.2
Absmax	20.1	14.4	10.4	45.7	54.6	58.6	25.4	15.9	11.8	42.9	47.6	48.5
Zigzag	17.1	13.4	8.6	46.6	<b>54.8</b>	58.1	<b>18.9</b>	<b>14.9</b>	10.9	<b>44.0</b>	<b>47.6</b>	49.6
MassDiff	<b>16.9</b>	<b>13.3</b>	<b>8.5</b>	<b>47.7</b>	54.2	<b>60.3</b>	<b>18.9</b>	<b>14.9</b>	<b>10.8</b>	<b>44.0</b>	47.0	<b>49.9</b>

pipelines, Qronos consistently outperforms GPTQ. However, when learning full-vector rotations, RTN consistently outperforms both. Thus, MixQuant\* corresponds to “MassDiff + QuaRot + Qronos” while MixQuant† corresponds to “MassDiff + SpinQuant + RTN”. These results highlight the complex interactions between rounding, rotation optimization, and permutation-based equalization. We leave a deeper investigation into this interaction for future work.

Table 6: We report WikiText2 perplexity and zero-shot accuracy for different compositions of Stage 1 (permutation and rotation) and Stage 2 (rounding) methods, following the pipeline illustrated in Figure 2.

Stage 1	Stage 2	Llama3						Qwen3					
		WikiText2 (↓)			0-shot (↑)			WikiText2 (↓)			0-shot (↑)		
1B	3B	8B	1B	3B	8B	1.7B	4B	8B	1.7B	4B	8B		
<b>MassDiff +QuaRot</b>	RTN	38.0	22.0	12.0	41.8	48.4	54.0	58.0	27.0	16.1	38.0	38.7	47.9
	GPTQ	28.4	14.9	9.8	44.9	52.5	58.9	25.8	21.0	12.6	43.4	37.9	49.3
	Qronos	<b>16.9</b>	<b>13.3</b>	<b>8.5</b>	<b>47.7</b>	<b>54.2</b>	<b>60.3</b>	<b>18.9</b>	<b>14.9</b>	<b>10.8</b>	<b>44.0</b>	<b>47.0</b>	<b>49.9</b>
<b>MassDiff +SpinQuant</b>	RTN	<b>15.9</b>	<b>10.9</b>	<b>8.4</b>	46.8	<b>56.1</b>	<b>60.9</b>	<b>13.6</b>	<b>11.1</b>	<b>9.5</b>	<b>45.8</b>	46.7	<b>50.7</b>
	GPTQ	19.5	13.4	9.2	46.2	55.5	60.5	20.8	17.5	12.8	42.5	41.4	47.5
	Qronos	16.4	13.2	8.5	<b>48.4</b>	55.9	59.7	18.2	14.7	10.6	44.5	<b>47.4</b>	50.2

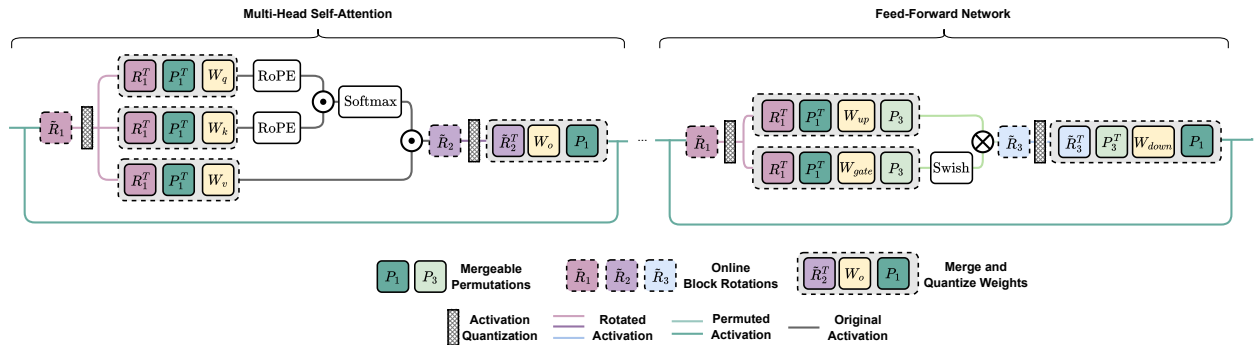


Figure 8: We provide an alternative quantization graph architecture where all rotations are left online, as proposed in [3]. We still merge permutations wherever possible and quantize the weights and activations for all linear layers.

**Merging Rotations.** The quantization graph architecture originally proposed for MR-GPTQ by Egiazarian *et al.* [3] exclusively applies online block Hadamard rotations (*i.e.*, no rotations are merged). In contrast, throughout our main experiments we study the quantization graph architecture illustrated in Figure 6, where rotations are merged into linear layers wherever possible in order to minimize changes to the deployed compute graph. Figure 8 illustrates the alternative graph architecture, in which all rotations are online block Hadamard rotations but where permutation-equivariant regions can still be equalized and permutations can be merged prior to deployment. In this architecture, MR-GPTQ corresponds to  $P_1 = P_3 = I_d$ . To isolate the impact of this architectural choice, we evaluate both graph variants across data formats and report results in Table 7, where “merged” refers to the graph in Figure 6 and “online” refers to the graph in Figure 8. In both graph architectures, all block rotations use  $b = 32$ . Since learning full-vector rotations in the online setting would incur significant deployment overhead, we do not evaluate an online variant of MixQuant† in this ablation. Nevertheless, MixQuant† consistently yields the highest quality models.

Table 7: We report WikiText2 perplexity and average zero-shot accuracy across data formats for “merged” and “online” quantization graph architectures for MR-GPTQ and MixQuant.

Format	Method	Graph	Llama3						Qwen3					
			WikiText2 (↓)			0-shot (↑)			WikiText2 (↓)			0-shot (↑)		
			1B	3B	8B	1B	3B	8B	1.7B	4B	8B	1.7B	4B	8B
INT4	MR-GPTQ	Merged	2e3	6e3	7e3	35.1	34.9	35.1	9e2	2e2	79.5	35.3	36.3	36.5
		Online	2e3	5e3	9e3	35.2	35.1	34.9	6e2	1e3	2e2	35.6	35.8	35.4
	MixQuant*	Merged	16.9	13.3	8.5	47.7	54.2	60.3	18.9	14.9	10.8	44.0	47.0	49.9
		Online	26.6	13.4	9.1	39.5	51.7	53.7	20.4	17.5	12.8	44.0	45.8	46.7
FP4	MR-GPTQ	Merged	15.9	10.9	8.4	46.8	56.1	60.9	13.6	11.1	9.5	45.8	46.7	50.7
		Online	43.2	27.0	18.9	42.6	47.0	50.7	60.0	2e2	93.0	38.0	37.5	39.2
	MixQuant*	Merged	22.8	14.9	11.1	44.6	51.1	57.2	31.1	1e2	41.8	39.5	36.8	39.9
		Online	21.0	16.6	10.6	44.2	51.6	54.9	21.4	16.6	12.0	42.4	45.5	47.7
MXFP4	MixQuant†	Merged	23.5	16.1	10.4	44.8	52.2	55.0	22.4	17.8	14.0	41.8	45.2	47.4
		Online	18.0	12.8	9.8	46.1	51.5	55.6	15.6	12.4	9.8	43.2	45.0	49.6
	MR-GPTQ	Merged	14.2	11.2	7.4	50.3	57.5	63.4	16.9	14.9	9.6	46.8	48.7	52.8
		Online	14.0	11.1	7.3	50.1	58.6	63.5	16.9	13.8	9.3	46.6	49.4	52.2
	MixQuant*	Merged	14.2	11.4	7.4	48.3	57.5	63.1	17.1	14.0	9.9	46.0	48.7	50.6
		Online	14.0	11.6	7.4	49.2	58.0	62.6	17.1	14.0	9.6	45.8	48.8	51.7
	MixQuant†	Merged	13.2	9.6	7.2	49.1	57.2	63.0	11.8	9.3	7.8	46.7	50.5	54.2

## D Proofs

### D.1 Proof of Proposition 3.1

**Proposition 3.1** (When Full-Vector Hadamard Rotations Suppress Outliers). *Let  $X \in \mathbb{R}^d$  be an activation vector, and let  $R \in \mathbb{R}^{d \times d}$  be a normalized Hadamard matrix. Define  $\delta = \|X\|_1 / (d\|X\|_\infty)$ , then the rotation of  $X$  by  $R$  satisfies*

$$\|XR\|_\infty \leq \delta\sqrt{d}\|X\|_\infty. \quad (1)$$

*Proof.* Given that  $\|X\|_1 = \delta d\|X\|_\infty$ , let  $R_i \in \mathbb{R}^d$  denote the  $i$ -th column in  $R$  for  $i \in [d]$ . Given that  $R$  is a normalized Hadamard matrix, it follows that  $\|R_i\|_\infty = 1/\sqrt{d}$ . One can bound  $|XR_i|$  via Hölder’s inequality [39] such that

$$|XR_i| \leq \|X\|_1\|R_i\|_\infty,$$

$$|XR_i| \leq \delta\sqrt{d}\|X\|_\infty,$$

for all  $i$ . Thus,  $\|XR\|_\infty \leq \delta\sqrt{d}\|X\|_\infty$ , concluding the proof.  $\square$

**Remark D.1** (Outlier Suppression and Energy Concentration for Full-Vector Hadamard Rotations). We can arrive at a similar inequality as Equation 1 with an alternate definition of  $\delta' = \|X\|_2 / (\sqrt{d}\|X\|_\infty)$ , which can be interpreted as the concentration of energy in  $X$ . Given that  $R$  is a normalized Hadamard matrix, it follows that  $\|R_i\|_2 = 1$  for  $i \in [d]$ . One similarly can bound  $|XR_i|$  via Hölder’s inequality [39] such that

$$|XR_i| \leq \|X\|_2\|R_i\|_2,$$

$$|XR_i| \leq \delta'\sqrt{d}\|X\|_\infty,$$

for all  $i$ . Thus,  $\|XR\|_\infty \leq \delta'\sqrt{d}\|X\|_\infty$ . Since  $\|X\|_\infty \leq \|X\|_2 \leq \sqrt{d}\|X\|_\infty$ , we have  $\delta' \in [\sqrt{d^{-1}}, 1]$ . This bound therefore states that only in the extreme case of  $\delta' = 1/\sqrt{d}$  are rotations guaranteed to not make outliers worse (*i.e.*,  $\|XR\|_\infty \leq \|X\|_\infty$ ). Therefore, unlike mass concentration, energy concentration does not deterministically yield a sufficient condition for outlier suppression with Hadamard rotations.

### D.2 Proof of Proposition 3.3

**Proposition 3.3** (When Block Hadamard Rotations Suppress Outliers). *Let  $\tilde{R} = I_n \otimes R$  be a block rotation, where  $R \in \mathbb{R}^{b \times b}$  is a normalized Hadamard matrix and  $\tilde{R} \in \mathbb{R}^{d \times d}$  with  $d = nb$ . Let  $X_{\{j\}} \in \mathbb{R}^b$  be the  $j$ -th block of activation vector  $X \in \mathbb{R}^d$  for  $j \in [n]$ . Define  $\delta_{\{j\}} = \|X_{\{j\}}\|_1 / (b\|X_{\{j\}}\|_\infty)$ , then the rotation of  $X$  by  $\tilde{R}$  satisfies*

$$\|X\tilde{R}\|_\infty \leq \max_{j \in [n]} \delta_{\{j\}} \sqrt{b}\|X_{\{j\}}\|_\infty. \quad (2)$$

*Proof.* Given that block rotation  $\tilde{R} = I_n \otimes R = \text{diag}(R, \dots, R)$  is an orthonormal block-diagonal matrix composed of  $n$  copies of a normalized Hadamard matrix  $R \in \mathbb{R}^{b \times b}$ , it follows that

$$\|X\tilde{R}\|_\infty = \max_j \|X_{\{j\}}R\|_\infty,$$

where  $X_{\{j\}} \in \mathbb{R}^b$  is the  $j$ -th block of input activation vector  $X \in \mathbb{R}^d$ .

Given that  $\|X_{\{j\}}\|_1 = \delta_{\{j\}}b\|X_{\{j\}}\|_\infty$ , let  $R_i \in \mathbb{R}^b$  denote the  $i$ -th column in  $R$  with  $i = 1, \dots, b$ . Given that  $\|R_i\|_\infty = 1/\sqrt{b}$ , one can follow Proposition 3.1 to bound  $|X_{\{j\}}R_i|$  via Hölder's inequality [39] such that

$$\begin{aligned} |X_{\{j\}}R_i| &\leq \|X_{\{j\}}\|_1\|R_i\|_\infty, \\ |X_{\{j\}}R_i| &\leq \delta_{\{j\}}\sqrt{b}\|X_{\{j\}}\|_\infty, \end{aligned}$$

for all  $i = 1, \dots, b$ . Thus,  $\|X\tilde{R}\|_\infty = \max_{j \in [n]} \|X_{\{j\}}R\|_\infty \leq \max_{j \in [n]} \delta_{\{j\}}\sqrt{b}\|X_{\{j\}}\|_\infty$ , concluding the proof.  $\square$

**Remark D.2** (Outlier Suppression and Energy Concentration for Block Hadamard Rotations). Building from Remark D.1, let  $\delta'_{\{j\}} = \|X_{\{j\}}\|_2/(\sqrt{b}\|X_{\{j\}}\|_\infty)$ . One can similarly bound  $|X_{\{j\}}R_i|$  such that

$$\begin{aligned} |X_{\{j\}}R_i| &\leq \|X_{\{j\}}\|_2\|R_i\|_2, \\ |X_{\{j\}}R_i| &\leq \delta'_{\{j\}}\sqrt{b}\|X_{\{j\}}\|_\infty, \end{aligned}$$

for all  $i = 1, \dots, b$ . Thus,  $\|X\tilde{R}\|_\infty = \max_{j \in [n]} \|X_{\{j\}}R\|_\infty \leq \max_{j \in [n]} \delta'_{\{j\}}\sqrt{b}\|X_{\{j\}}\|_\infty$ , where  $\delta'_{\{j\}} \in [\sqrt{b^{-1}}, 1]$  for all  $j \in [n]$ . This further implies that, unlike mass concentration, energy concentration does not deterministically yield a sufficient condition for outlier suppression with block Hadamard rotations.

### D.3 Proof of Corollary 3.4

**Corollary 3.4** (Deterministic Evolution of Post-Rotation Outliers). *Let  $X \in \mathbb{R}^d$  be an activation vector and let  $X_{\{j\}} \in \mathbb{R}^b$  be the  $j$ -th block of  $X$  for  $j \in [n]$  with  $d = nb$ . Define  $\mathcal{Z}(b; X) = \max_{j \in [n]} \sqrt{b} \delta_{\{j\}}\|X_{\{j\}}\|_\infty$ , where  $\delta_{\{j\}} = \|X_{\{j\}}\|_1 / (b\|X_{\{j\}}\|_\infty)$ . Then, for positive integers  $k, b' \in \mathbb{N}$  such that  $b = kb'$ , it is verified that*

$$\mathcal{Z}(b; X) \leq \sqrt{k} \mathcal{Z}(b'; X)$$

*Proof.* Given that  $\|X_{\{j\}}\|_1 = \delta_{\{j\}}b\|X_{\{j\}}\|_\infty$ , where  $X_{\{j\}} \in \mathbb{R}^b$  denotes the  $j$ -th block of  $X \in \mathbb{R}^d$  with  $d = nb$ , let  $X_{\{j,i\}} \in \mathbb{R}^{b'}$  denote the  $i$ -th sub-block of  $X_{\{j\}}$  for  $i \in [k]$  with  $b = kb'$ . Then,

$$\begin{aligned} \mathcal{Z}(b; X) &= \max_{j \in [n]} \delta_{\{j\}}\sqrt{b}\|X_{\{j\}}\|_\infty = \max_{j \in [n]} \|X_{\{j\}}\|_1/\sqrt{b} \\ &= \max_{j \in [n]} \left( \sum_{i \in [k]} \|X_{\{j,i\}}\|_1 \right) / \sqrt{kb'} \\ &\leq \max_{j \in [n], i \in [k]} \sqrt{\frac{k}{b'}} \|X_{\{j,i\}}\|_1 = \sqrt{k} \mathcal{Z}(b'; X) \end{aligned}$$

Thus,  $\mathcal{Z}(b; X) \leq \sqrt{k} \mathcal{Z}(b'; X)$ , concluding the proof.  $\square$

### D.4 Proof of Proposition 3.5

We first state two auxiliary lemmas for completeness; both are well-known consequences of Hoeffding's lemma [40].

**Lemma D.3** (Rademacher Signed Sum is Sub-Gaussian, cf. Section 2.5 [40]). *Given  $Y = (Y_1, \dots, Y_d) \in \mathbb{R}^d$ , let  $S_1, \dots, S_d$  be independent Rademacher random variables such that  $S_i \sim \text{Rad}(\pm 1)$ , and define  $Z = \sum_{i=1}^d S_i Y_i$ . Then for all  $t \in \mathbb{R}$ ,*

$$\mathbb{E}[e^{tZ}|Y] \leq \exp\left(\frac{t^2\|Y\|_2^2}{2}\right).$$

*In particular, conditional on  $Y$ , the random variable  $Z$  is sub-Gaussian with variance proxy  $\|Y\|_2^2$ .*

**Lemma D.4** ( $\ell_\infty$  Concentration from Conditional Sub-Gaussian, cf. Theorem 2.6.2 [40]). *Let  $V = (V_1, \dots, V_d) \in \mathbb{R}^d$  be a random vector and let  $Y$  be a (possibly random) vector. Assume that, conditional on  $Y$ , each  $V_i$  is zero-mean and sub-Gaussian with variance proxy  $\nu_i^2(Y)$  in the sense that*

$$\mathbb{E}[e^{tV_i} | Y] \leq \exp\left(\frac{t^2 \nu_i^2(Y)}{2}\right) \quad \text{for all } t \in \mathbb{R}.$$

Then, conditional on  $Y$ , for all  $\tau \geq 0$ ,

$$\mathbb{P}(\|V\|_\infty \geq \tau | Y) \leq 2 \sum_{i=1}^d \exp\left(-\frac{\tau^2}{2\nu_i^2(Y)}\right) \leq 2d \exp\left(-\frac{\tau^2}{2\nu_{\max}^2(Y)}\right),$$

where  $\nu_{\max}^2(Y) = \max_{i \in [d]} \nu_i^2(Y)$ .

To prove Proposition 3.5, we separately consider the sign and magnitude of activation vector  $X \in \mathbb{R}^d$  such that  $X = \text{sign}(X) \odot |X| = S \odot Y$ , then model  $S = (S_1, \dots, S_d)$  as a random vector with i.i.d. Rademacher entries,  $S_i \sim \text{Rad}(\pm 1)$ . As such, we clarify two core assumptions: (1) we assume  $\mathbb{P}_S[+1 | Y] = \mathbb{P}_S[-1 | Y] = 0.5$ , and (2) we assume each entry  $S_i$  is i.i.d. Rademacher across vector coordinates within each activation vector. To ensure these assumptions are reasonable, we empirically evaluate Qwen3 1.7B using WikiText2. First, we find that the fraction of positive signs within a vector concentrates tightly around 0.5, with a minimum of 0.47, a max of 0.53, and a mean of 0.50 across tokens and layers. Second, we find that the pairwise correlations of  $S_i$  for  $i \in [d]$  are close to a Rademacher baseline estimated over 128 tokens; the off-diagonals of  $\mathbb{E}_{S|Y}[S^T S]$  have a standard deviation that ranges between 0.08 and 0.09 across layers, where a Rademacher distribution would yield  $1/\sqrt{128} = 0.088$ . Thus, having verified our assumptions are reasonable, we proceed with proving Proposition 3.5 using Lemmas D.3 and D.4.

**Proposition 3.5** (Probabilistic Evolution of Post-Rotation Outliers). *Let  $\tilde{R} = I_n \otimes R$  be a block rotation, where  $R \in \mathbb{R}^{b \times b}$  is a normalized Hadamard matrix and  $\tilde{R} \in \mathbb{R}^{d \times d}$  with  $d = nb$ . Given  $Y = (Y_1, \dots, Y_d) \in \mathbb{R}^d$ , let  $S = (S_1, \dots, S_d)$  be a random vector with i.i.d. Rademacher entries  $S_i \sim \text{Rad}(\pm 1)$ . Define activation vector  $X \in \mathbb{R}^d$  coordinate-wise as  $X_i = S_i Y_i$  for  $i \in [d]$ . Then, conditional on  $Y$ ,*

$$\|X \tilde{R}\|_\infty \leq \sqrt{\frac{2}{b} \log\left(\frac{2d}{\varepsilon}\right)} \|X\|_2^2 \quad (3)$$

with probability at least  $1 - \varepsilon$ .

*Proof.* Let  $\tilde{R} = I_n \otimes R$  be a block rotation, where  $R \in \mathbb{R}^{b \times b}$  is a normalized Hadamard matrix with entries  $R_{u,v} = \{\pm 1/\sqrt{b}\}$  for all  $u, v \in [b]$ , and  $\tilde{R} \in \mathbb{R}^{d \times d}$  with  $d = nb$ . Given  $Y = (Y_1, \dots, Y_d) \in \mathbb{R}^d$ , let  $S = (S_1, \dots, S_d)$  be a random vector with i.i.d. Rademacher entries  $S_i \sim \text{Rad}(\pm 1)$ . Define activation vector  $X \in \mathbb{R}^d$  coordinate-wise as  $X_i = S_i Y_i$  for  $i \in [d]$ ; note that  $|X_i| = |Y_i|$  for all  $i$ . Let  $\tilde{X} = X \tilde{R}$  be the result of rotating  $X$  by  $\tilde{R}$ .

Define block index  $\beta(i) = \lceil i/b \rceil$  with corresponding index set  $\mathcal{B}_{\beta(i)} = \{(\beta(i)-1)b+1, \dots, \beta(i)b\}$ . Since  $\tilde{R} = I_n \otimes R$  with  $R \in \mathbb{R}^{b \times b}$ , the  $i$ -th coordinate of  $\tilde{X}$  is then

$$\tilde{X}_i = \sum_{k \in [d]} S_k Y_k \tilde{R}_{k,i} = \sum_{k \in \mathcal{B}_{\beta(i)}} S_k Y_k \tilde{R}_{k,i}.$$

For  $k \in \mathcal{B}_{\beta(i)}$ , write  $\tilde{R}_{k,i} = \frac{1}{\sqrt{b}} \gamma_{k,i}$  with  $\gamma_{k,i} \in \{\pm 1\}$ , and define  $S_k^{(i)} = \gamma_{k,i} S_k$ . Since  $\gamma_{k,i}$  is fixed and  $S_k \sim \text{Rad}(\pm 1)$ , it follows that  $S_k^{(i)}$  remain i.i.d. Rademacher for  $k \in \mathcal{B}_{\beta(i)}$ . Hence,

$$\tilde{X}_i = \frac{1}{\sqrt{b}} \sum_{k \in \mathcal{B}_{\beta(i)}} S_k^{(i)} Y_k.$$

Then, from Lemma D.3, it follows that, conditional on  $Y$ ,  $\tilde{X}_i$  is sub-Gaussian with variance proxy  $\|Y_{\{\beta(i)\}}\|_2^2/b$ , where  $Y_{\{\beta(i)\}}$  denotes block  $\beta(i)$  of  $Y$  and  $\beta(i) \in [n]$ . In particular, since  $|Y_k| = |X_k|$  for all  $k \in \mathcal{B}_{\beta(i)}$ ,

$$\mathbb{E}[e^{t\tilde{X}_i} | Y] \leq \exp\left(\frac{t^2 \|X_{\{\beta(i)\}}\|_2^2}{2b}\right),$$

where  $X_{\{\beta(i)\}}$  similarly denotes block  $\beta(i)$  of  $X$ .

Since  $S_i$  are zero-mean conditional on  $Y$ , it follows from Lemma D.4 that

$$\mathbb{P} \left( \|X\tilde{R}\|_\infty \geq \tau \mid Y \right) \leq 2d \exp \left( - \frac{b\tau^2}{2 \max_{j \in [n]} \|X_{\{j\}}\|_2^2} \right).$$

Solving for  $\tau$  such that  $\mathbb{P} \left( \|X\tilde{R}\|_\infty \geq \tau \mid Y \right) \leq \varepsilon$ , it follows that

$$\begin{aligned} 2d \exp \left( - \frac{b\tau^2}{2 \max_{j \in [n]} \|X_{\{j\}}\|_2^2} \right) &\leq \varepsilon \\ \frac{b\tau^2}{2 \max_{j \in [n]} \|X_{\{j\}}\|_2^2} &\geq \log \left( \frac{2d}{\varepsilon} \right) \\ \tau &\geq \sqrt{\frac{2}{b} \log \left( \frac{2d}{\varepsilon} \right) \max_{j \in [n]} \|X_{\{j\}}\|_2^2} \end{aligned} \tag{6}$$

Therefore, conditional on  $Y$  and with

$$\tau = \sqrt{\frac{2}{b} \log \left( \frac{2d}{\varepsilon} \right) \max_{j \in [n]} \|X_{\{j\}}\|_2^2},$$

we obtain

$$\|X\tilde{R}\|_\infty \leq \sqrt{\frac{2}{b} \log \left( \frac{2d}{\varepsilon} \right) \max_{j \in [n]} \|X_{\{j\}}\|_2^2} \leq \sqrt{\frac{2}{b} \log \left( \frac{2d}{\varepsilon} \right) \|X\|_2^2}$$

with probability at least  $1 - \varepsilon$ , concluding the proof.  $\square$

**Remark D.5** (Probabilistic Analysis of Outlier Suppression). Proposition 3.5 provides a complementary geometric perspective to the outlier suppression capabilities of block Hadamard rotations, namely that outlier suppression is probabilistically limited by the block with the largest mass. Recall the well-known relationship between mass and energy: for  $X \in \mathbb{R}^d$ , it can be shown that  $\|X\|_2 \leq \|X\|_1$  via

$$\|X\|_1^2 = \left( \sum_{i \in [d]} |X_i| \right)^2 = \sum_{i \in [d]} X_i^2 + \sum_{i \in [d]} \sum_{j \in [d] \setminus i} |X_i||X_j| \geq \sum_{i \in [d]} X_i^2 = \|X\|_2^2.$$

It therefore follows from Proposition 3.5 that, conditional on  $Y$ , Equation 3.5 can be further bounded as

$$\begin{aligned} \|X\tilde{R}\|_\infty &\leq \sqrt{\frac{2}{b} \log \left( \frac{2d}{\varepsilon} \right) \max_{j \in [n]} \|X_{\{j\}}\|_2^2} \\ &\leq \sqrt{\frac{2}{b} \log \left( \frac{2d}{\varepsilon} \right) \max_{j \in [n]} \|X_{\{j\}}\|_1^2} = \sqrt{2 \log \left( \frac{2d}{\varepsilon} \right) \max_{j \in [n]} \delta_{\{j\}} \sqrt{b} \|X_{\{j\}}\|_\infty} \end{aligned}$$

with probability of at least  $1 - \varepsilon$ , where  $\delta_{\{j\}} = \|X_{\{j\}}\|_1 / (b \|X_{\{j\}}\|_\infty)$ . Importantly, while this reduction again shows that outlier suppression is limited by the block with the largest mass, it does not yield a sufficient condition under which outlier suppression is guaranteed. Furthermore, building from Remarks D.1 and D.2, one can arrive at a similar insight using the energy concentration metric  $\delta'_{\{j\}} = \|X_{\{j\}}\|_2 / (\sqrt{b} \|X_{\{j\}}\|_\infty)$ .